JACS
JOURNAL OF THE AMERICAN CHEMICAL SOCIETY
pubs.acs.org/JACS
Article

Speciation of Lanthanide Metal Ion Dopants in Microcrystalline All-Inorganic Halide Perovskite $CsPbCl_3$

Dominik J. Kubicki,* Daniel Prochowicz, Albert Hofstetter, Amita Ummadisingu, and Lyndon Emsley*

Cite This: J. Am. Chem. Soc. 2024, 146, 9554−9563
Read Online

ABSTRACT: Lanthanides are versatile modulators of optoelectronic properties owing to their narrow optical emission spectra across the visible and near-infrared range. Their use in metal halide perovskites (MHPs) has recently gained prominence, although their fate in these materials has not yet been established at the atomic level. We use cesium-133 solid-state NMR to establish the speciation of all nonradioactive lanthanide ions (La^{3+}, Ce^{3+}, Pr^{3+}, Nd^{3+}, Sm^{3+}, Sm^{2+}, Eu^{3+}, Eu^{2+}, Gd^{3+}, Tb^{3+}, Dy^{3+}, Ho^{3+}, Er^{3+}, Tm^{3+}, Yb^{3+}, Lu^{3+}) in microcrystalline $CsPbCl_3$. Our results show that all lanthanides incorporate into the perovskite structure of $CsPbCl_3$ regardless of their oxidation state (+2, +3).

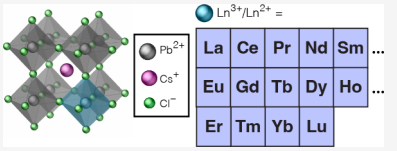

INTRODUCTION

Lead halide perovskites have attracted significant attention as semiconducting materials for optoelectronic applications.[1] Within this class of material, cesium lead halide ($CsPbX_3$, X = Cl, Br, I) nanocrystals have been widely used for light emitting diodes (LEDs) and solar cell applications, offering a viable alternative to classical II−VI metal chalcogenides.[2−6] Doping of $CsPbX_3$ materials with metal ions is an effective way of tuning their optoelectronic response (emission wavelength and photoluminescence quantum yield) and stability. Rare earth metal ions, specifically lanthanides, have been particularly appealing as dopants owing to their sharp emission spectra which extend down to the near-infrared (NIR) region. This property makes them suitable for NIR and white LEDs, emitters, photodetectors, in addition to application in counterfeit security measures, optical temperature sensing, and optical data encoding.[7−15] Various combinations of lanthanides have been introduced to halide perovskites, mostly in the form of nanocrystals, to tune their properties.[12,16−24] These explorations build on the use of lanthanide doping in other classes of phosphor materials, typically oxides, silicates, and phosphates, which have been underway since at least the early 1940s when efficient luminescence of Eu^{2+} doped phosphors was observed under UV excitation.[25,26] Halide perovskite phosphors doped with lanthanides have also recently been reported.[27]

Knowledge of the speciation of lanthanides in host matrices is essential to understand how they incorporate since the local structure of the dopant and its homogeneity within the host determine its optical properties.[28] In the case of lanthanides with a partially filled 4f subshell, solid-state NMR[29] has been particularly useful to study their incorporation into inorganic materials, including phosphors, because their paramagnetism leads to substantial changes in the NMR shifts and relaxation properties of the host.[30−35] More generally, paramagnetic NMR techniques have been essential for studying atomic-level structure in areas such as battery materials,[36] pharmaceuticals,[37] metalloproteins,[38] porous solids,[39] optoelectronic materials,[40] and polymers.[41,42] Despite the growing use of solid-state NMR to determine speciation in MHPs[43] and despite the importance of lanthanides in metal halide perovskites, their atomic-level speciation in metal halide perovskites has remained largely unexplored.[7] Xiang et al. first explored lanthanide speciation in metal halide perovskites and found that Eu^{2+} has the capacity to incorporate into $CsPbI_2Br$ enhancing its efficiency in solar cells.[44] Very recently, Xu et al. have used aberration-corrected atomic-resolution scanning transmission electron microscopy and three-dimensional atom probe tomography to directly observe Yb^{3+} inside $CsPbCl_3$ nanocrystals.[24]

Here we focus our attention on the host material most widely used in light emission studies, cesium lead chloride, $CsPbCl_3$.[45] We set out to answer the following question: do all rare earth ions have the capacity to mix with $CsPbCl_3$ at the atomic level? The answer to this question is not obvious since there are no rigorous rules for predicting the incorporation of dopants into halide perovskites and, more generally, the formation of solid solutions in extended solids. Empirical rules have been successful but have limited reliability in complex systems. Some prominent examples of phenomenological prediction of phase equilibria are the Hume−Rothery rules for multicomponent alloys,[46] the computational CALPHAD methodology applicable to other types of solids,[47] and the Goldschmidt tolerance factor for perovskites.[48,49] Machine learning (ML)-based approaches are currently gaining

Received: October 16, 2023
Revised: March 22, 2024
Accepted: March 25, 2024
Published: March 28, 2024

prominence.[50] While the question of lanthanide doping in $CsPbCl_3$ has been explored for some lanthanides using long-range structure characterization techniques (XRD, TEM),[7,51] dopants do not typically form periodic structures in the host matrix. Therefore, the complementary use of local structure characterization techniques is essential to identifying their location. A number of recent examples have shown that predicting the speciation of dopants in halide perovskites is nontrivial.[43] For example, the incorporation of Co^{2+} into $MAPbI_3$ (MA = methylammonium)[52] was proposed but solid-state NMR investigations have shown that it is not the case.[53] Grey et al. used paramagnetic effects in solid-state NMR to demonstrate the limited miscibility of $Y_2Sn_2O_7$ and $Nd_2Sn_2O_7$ pyrochlores.[30] Finally, the speciation of potassium and guanidinium ions in hybrid halide perovskites had been subject to a long-standing debate that was settled using solid-state NMR.[54,55]

Here we determine a comprehensive understanding of the entire lanthanide dopant space in $CsPbCl_3$ developed using ^{133}Cs NMR. Unlike common materials characterization strategies, this technique offers the advantage of being sensitive to the structure topology, local symmetry, halide composition, and doping of the perovskite host.[43,56,57] Paramagnetic rare earth metal ions are expected to induce paramagnetic relaxation enhancements (PRE) of the otherwise diamagnetic perovskite host matrix, leading to shortening of the ^{133}Cs longitudinal relaxation times.[30,35,58] In addition, the interaction between the unpaired 4f electrons of the lanthanide and the ^{133}Cs nuclei may cause the resonance frequency of the latter to shift.[30,58] The diamagnetic lanthanides (La^{3+} and Lu^{3+}), if incorporated, may affect ^{133}Cs shifts by inducing local lattice distortions.[43] They may also affect ^{133}Cs T_1 relaxation, which in $CsPbCl_3$ is driven by the modulation of dipolar couplings with the neighboring nuclei,[59] because ^{139}La and ^{175}Lu are 99.9% and 97.4% abundant, respectively, and therefore are expected to couple magnetically with ^{133}Cs.

Here, we exploit these ideas to understand the speciation of rare earth metal ions in this gold standard light emitting halide perovskite. We first report a facile solid-state route to microcrystalline $CsPbCl_3$ doped with lanthanides (Ln^{n+} = Ce^{3+}, Pr^{3+}, Nd^{3+}, Sm^{3+}, Sm^{2+}, Eu^{3+}, Eu^{2+}, Gd^{3+}, Tb^{3+}, Dy^{3+}, Ho^{3+}, Er^{3+}, Tm^{3+}, Yb^{3+}, Lu^{3+}) and then use cesium-133 solid-state NMR to demonstrate their successful incorporation into the perovskite structure.

EXPERIMENTAL SECTION

Materials. The following materials were used in this study: CsCl (Sigma, 99.999%), $PbCl_2$ (Sigma, 99.999%, anhydrous), $LaCl_3$ (Sigma, >99.99%, anhydrous), $CeCl_3$ (Sigma, 99.99%, anhydrous), $PrCl_3$ (Sigma, 99.99%, anhydrous), $NdCl_3$ (AlfaAesar, 99.9%, anhydrous), $SmCl_3$ (Sigma, 99.9%, anhydrous), SmI_2 (Sigma, 99.9%, anhydrous), $EuCl_3$ (Sigma, 99.99%, anhydrous), EuI_2 (Sigma, 99.999%, anhydrous), $GdCl_3$ (Sigma, 99.99%, anhydrous), $TbCl_3$ (Sigma, 99.99%, anhydrous), $DyCl_3$ (Sigma, 99.99%, anhydrous), $HoCl_3$ (Sigma, 99.9%, anhydrous), $ErCl_3$ (Sigma, 99.9%, ultra dry), ErI_3 (abcr, 99.9%, anhydrous), $TmCl_3$ (Sigma, 99.9%, anhydrous), $YbCl_3$ (Sigma, 99.99%, anhydrous), $LuCl_3$ (Sigma, 99.99%, anhydrous).

Perovskite Mechanosynthesis. Starting materials were stored inside a glovebox in dry nitrogen at room temperature. Microcrystalline perovskite powders were synthesized by grinding the reagents in an electric ball mill (Retsch Mixer Mill MM-200) for 30 min at 25 Hz using an agate grinding jar (10 mL) and an agate ball (⌀10 mm). We used agate jars to ensure that the reaction proceeds to completion (Figure S1). The resulting powders were annealed at 300 °C for 2 min. The following amounts of reagents were used. Undoped $CsPbCl_3$: CsCl (168 mg, 1 mmol), and $PbCl_2$ (278 mg, 1 mmol). For $CsPbCl_3$ doped with excess $Ln^{2+/3+}$ ions, the following amounts of lanthanide halides were added to a mixture of CsCl (168 mg, 1 mmol) and $PbCl_2$ (278 mg, 1 mmol): $LaCl_3$ (24 mg, 0.1 mmol), $CeCl_3$ (25 mg, 0.1 mmol), $PrCl_3$ (25 mg, 0.1 mmol), $NdCl_3$ (2.5, 25, and 50 mg, for 0.01, 0.1, and 0.2 mmol, respectively), $SmCl_3$ (26 mg, 0.1 mmol), SmI_2 (40 mg, 0.1 mmol), $EuCl_3$ (26 mg, 0.1 mmol), EuI_2 (41 mg, 0.1 mmol), $GdCl_3$ (26 mg, 0.1 mmol), $TbCl_3$ (27 mg, 0.1 mmol), $DyCl_3$ (27 mg, 0.1 mmol), $HoCl_3$ (27 mg, 0.1 mmol), $ErCl_3$ (27 mg, 0.1 mmol), ErI_3 (55 mg, 0.1 mmol), $TmCl_3$ (28 mg, 0.1 mmol), $YbCl_3$ (28 mg, 0.1 mmol), $LuCl_3$ (28 mg, 0.1 mmol).

NMR Measurements. Solid-state MAS NMR spectra of ^{133}Cs (65.6 MHz at 11.7 T) and ^{207}Pb (104.7 MHz at 11.7 T) were recorded on a Bruker Avance III 11.7 T spectrometer equipped with a 3.2 mm CPMAS probe. ^{133}Cs shifts were referenced to a 1 M aqueous solution of cesium chloride, using solid CsI (δ = 271.05 ppm) as a secondary reference.[60] ^{207}Pb chemical shifts were referenced to liquid $(CH_3)_4Pb$ using the chemical shift of $Pb(NO_3)_2$ as a secondary reference (δ_{iso} = −3494 ppm).[61] For the saturation−recovery experiments, saturation was achieved by applying a train of 30 $\pi/2$ pulses spaced by 3 ms. All measurements were carried out using identical conditions, i.e., at 22 kHz MAS rate with the sample temperature of ∼54 °C measured using the linear shift dependence of ^{79}Br on temperature (0.025 ppm/K) in solid KBr (Figure S16).[62] For the quantitative spectra, a recycle delay of 500 s was used for undoped $CsPbCl_3$, 200 s was used for the 10% doped materials, 60 s was used for the 20% Nd^{3+} doped material, and 5 s was used for Cs_4NdCl_6. The fast-recycling spectra were recorded with a recycling delay of 1 ms. Between 4 and 32 scans were used for the quantitative spectra and between 1024 and 256000 for the fast-recycling spectra. The link to all the raw data is https://zenodo.org/records/10853121. The saturation−recovery data were fitted in MATLAB using the stretched exponential function, and the fitted parameters are reported at the 95% confidence level (Supplementary Note 3).

Powder X-ray Diffraction. Powder XRD patterns of the materials were recorded by using a Panalytical Empyrean diffractometer with a Cu target (Kα1 = 1.540 56 Å) using background-free holders made of monocrystalline silicon. Variable-temperature powder XRD was recorded using Bruker D8 Advance diffractometer equipped with a high-temperature oven chamber (Anton Paar, HTK 1200N) using a Cu target. The link to the raw data is https://zenodo.org/records/10853121.

Scanning Transmission Electron Microscopy (STEM) Energy-Dispersive X-ray Spectroscopy (EDX). STEM EDX measurements were carried out on a Tecnai Osiris microscope at 200 kV by using the STEM mode and Super-X detector to acquire EDX elemental maps.

RESULTS AND DISCUSSION

Figure 1 schematically shows the materials prepared in this study. Lanthanide-doped $CsPbCl_3$ was prepared by solid-state mechanosynthesis with the addition of 10 mol % excess of rare earth chlorides with the lanthanide in the +3 oxidation state. In addition, in the cases of Sm and Eu, iodides with the lanthanide in the +2 oxidation state were also used. The materials were annealed to remove grinding-induced defects, and XRD showed that in all cases, essentially phase-pure perovskite structure has formed (Figure S2). The XRD peak positions were essentially unaffected within the measurement uncertainty relative to undoped $CsPbCl_3$. $CsPbCl_3$ exhibits three structural phase transitions near room temperature. The material is cubic above 47 °C (phase I), tetragonal between 47 and 42 °C (phase II), orthorhombic between 42 and 37 °C (phase III), and monoclinic below 37 °C (phase IV). Each of these phases is expected to have a slightly different ^{133}Cs shift. To obtain a meaningful comparison, it was essential to carry

https://doi.org/10.1021/jacs.3c11427
J. Am. Chem. Soc. 2024, 146, 9554−9563

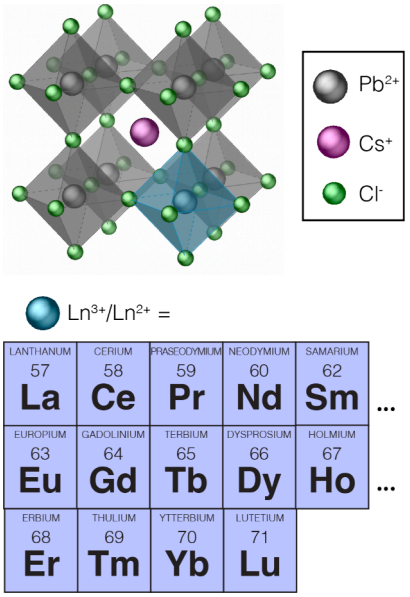

Figure 1. Schematic representation of the 3D perovskite structure of $CsPbCl_3$ doped with lanthanides (Ln^{n+} = La^{3+}, Ce^{3+}, Pr^{3+}, Nd^{3+}, Sm^{3+}, Sm^{2+}, Eu^{3+}, Eu^{2+}, Gd^{3+}, Tb^{3+}, Dy^{3+}, Ho^{3+}, Er^{3+}, Tm^{3+}, Yb^{3+}, and Lu^{3+}).

out the NMR experiments under identical conditions as spinning and gas flow inside the probe may affect the temperature of the sample and therefore the signal position (Figure S3). The sample temperature inside the rotor measured using the ^{79}Br shift of solid KBr was ca. 54 °C in all the measurements carried out, and as such, the material was in the cubic phase. XRD carried out on selected materials at 55 °C confirms that the presence of the dopants does not affect the crystal structure appreciably under the conditions of the MAS NMR experiment. Since the incorporation of dopants is expected to affect ^{133}Cs resonance frequencies and the T_1 relaxation of the corresponding species, we recorded ^{133}Cs spectra and saturation–recovery data for all of the materials.

We first focus on the effect of lanthanide doping on the ^{133}Cs T_1 relaxation. Figure 2 shows the ^{133}Cs T_1 values measured for undoped and doped $CsPbCl_3$ using a saturation–recovery sequence with the integral being taken across the whole spectrum. The saturation–recovery curves were fitted using a stretched exponential because a distribution of T_1 values is expected (see Supplementary Note 1 for details).[53] We observe T_1 shortening for all dopants, indicating that they modify the parent host structure. We rationalize the effect of the diamagnetic lanthanides (La^{3+} and Lu^{3+}) on ^{133}Cs T_1 by invoking the dipolar relaxation mechanism of ^{133}Cs in $CsPbCl_3$.[59] In the doped structures, the ^{133}Cs nuclei exhibit additional dipolar couplings to the nearly 100% abundant ^{139}La

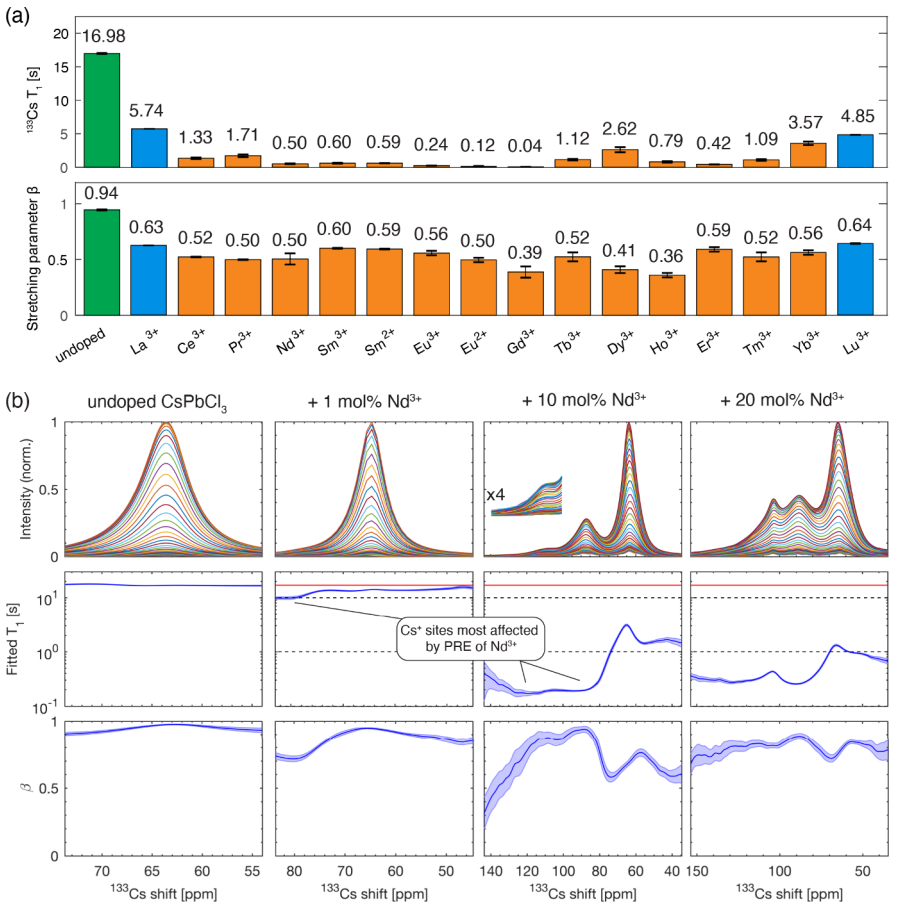

Figure 2. ^{133}Cs longitudinal relaxation time measurements in $CsPbCl_3$ doped with lanthanides. (a) Fitted longitudinal relaxation times, T_1, and stretching parameters, β, obtained for a fit to the integral of the whole spectrum. The fitting was carried out using the stretched exponential function (Supplementary Note 1). (b) Distribution of the fitted T_1 and β values across the spectrum for different Nd^{3+} loadings (0, 1, 10, and 20%). The top panels show an overlay of the saturation–recovery spectra for different recovery times.

https://doi.org/10.1021/jacs.3c11427
J. Am. Chem. Soc. 2024, 146, 9554–9563

and ^{175}Lu nuclei, and we expect that the modulation of these dipolar couplings leads to the experimentally observed ∼3 times faster T_1 relaxation. As expected, the T_1 shortening in the case of paramagnetic lanthanides is more substantial (5 times faster for Yb^{3+} and 425 times faster for Gd^{3+}) and related to the PRE effect. This effect is caused by the through-space dipolar interaction between the ^{133}Cs nuclei and the unpaired 4f electrons. Efficient nuclear relaxation occurs as a result of the modulation of this interaction at frequencies on the order of the ^{133}Cs Larmor frequency (104 MHz at 11.7 T, corresponding to correlation times on the order of 10 ns), and since the strength of this interaction scales as $1/r^6$, it is a direct local probe of the presence of the paramagnetic species within the host structure. In all cases the recovery is stretched, indicating that there is a distribution of T_1 values within the material.[63] The stretching factor, β, is 0.6 for Lu^{3+} and La^{3+}, and it is 0.4−0.6 for paramagnetic lanthanides. For a host matrix with randomly distributed paramagnetic dopants and in the absence of spin diffusion, it has been shown theoretically and experimentally that the stretching parameter β takes on a value of 0.5.[63−65] This result is a strong indication that (a) for 10 mol % Ln^{3+} doping, the lanthanides are randomly distributed within the host matrix, and (b) ^{133}Cs−^{133}Cs spin diffusion is essentially absent. While ^{133}Cs is 100% abundant, we conclude that its low gyromagnetic ratio and the relatively large intercesium spacings renders spin diffusion negligible on the relaxation time scale here.[66] Because there is a distribution of local environments with distinct T_1 values, we next show how those values vary across the inhomogeneously broadened spectrum for Nd^{3+} when its content increases from 0 to 20 mol % (Figure 2b).

The T_1 of undoped $CsPbCl_3$ is uniform across the entire peak with $\beta \approx 1$ (β decreases slightly on both sides of the signal possibly because these regions might contain contributions from grain boundaries, which are known to exhibit faster relaxation,[67] hence the slightly broader distribution of T_1 values in these regions). For 1 mol % Nd^{3+}, while there is very little change to the line shape, it is clear that the T_1 decreases across the resonance, with the local environments at higher frequencies being affected the most. The β value for those environments decreases to ∼0.7. A spectrum recorded using a very short recycle delay enhances the intensity of these fast-relaxing environments and shows that there is a new local Cs^+ environment already present at this low doping ratio (Figure S4). For 10 mol % Nd^{3+}, there is a substantial drop in T_1 across the entire line shape, and two distinct peaks appear at higher frequencies relative to the initial peak. These signals manifestly correspond to Cs^+ sites near Nd^{3+} because of the substantial PRE associated with them. The main peak is now fully affected by PRE, which means that all Cs^+ sites within the material sense the presence of Nd^{3+} through the $1/r^6$ relationship (as spin diffusion is negligible on this time scale for ^{133}Cs, as mentioned above).[66] This result is expected based on the binomial law:[68] for 10 mol % Nd^{3+}, the probability of encountering a Cs^+ site with 0 Nd^{3+} nearest neighbors in a 10 Å radius is less than 1%, assuming a random dopant distribution. This result therefore also indicates that there is no substantial Nd^{3+} clustering, which would lead to the presence of Nd^{3+} deficient regions unaffected by PRE within the material, in agreement with the interpretation of the experimentally observed $\beta = 0.5$.

Interestingly, while the average β for this sample is 0.5 (Figure 2a), the spectrally resolved β fitting in Figure 2b shows that there is a distribution of β values across the line shape. We interpret this result as follows: because each spectral region corresponds to Cs^+ sites at a different distance from the paramagnetic dopant, the local distribution of T_1 for each spectral region is slightly different, leading to different β values. For 20 mol % Nd^{3+}, the PRE increases still further, with the T_1 being less than 1 s over nearly the entire line shape. It is noteworthy that β takes on values between 0.7 and 0.8 across the spectrum in this material, which again corroborates the conclusion that there is no ^{133}Cs−^{133}Cs spin diffusion. Efficient spin diffusion in a material with such high concentration of paramagnetic dopants would lead to $\beta = 1$.[69] We have carried out an analogous analysis for the other materials doped with paramagnetic lanthanides, and in all cases the new peaks are strongly affected by PRE (see the Supporting Information section "Data fitting results"). It is worth noting that there is a continuum of apparent T_1 values on going from the low frequency side of the spectrum (weaker PRE) to the high frequency side (stronger PRE). The gradual change in the apparent T_1 indicates that each of the peaks is a convolution of many local environments with slightly different distances to the paramagnetic ion, and as a result, the spectrum is inhomogeneously broadened. Finally, we also note that intermediate β values ($0.5 < \beta < 1$) have also been observed in some materials (for average β, i.e. fitted for the whole spectrum simultaneously), such as silicon carbide.[70] Those cases have been interpreted in terms of the inhomogeneous distribution of paramagnetic impurities. Taken together, the ^{133}Cs T_1 relaxation analysis shows that all the lanthanide ions incorporate into the host matrix and, for 10 mol % Ln^{3+} doping, are randomly distributed. This result is corroborated by the STEM EDX maps of selected materials, which show that the distribution of Cs and the lanthanides is highly uniform within the perovskite grains (Figures S20−22). Our results agree with those in a recent study by Xu et al., who used 3D atom probe tomography to study an Yb-doped $CsPbCl_3$ single crystal and concluded that the dopant distribution in their material also is highly uniform.[24]

We next analyzed the quantitative ^{133}Cs spectra (Figure 3). The ^{133}Cs signal of undoped $CsPbCl_3$ is narrow (full width at half maximum, FWHM, ∼85 Hz, 1.3 ppm) and nearly symmetrical. When $CsPbCl_3$ is doped with 10 mol % lanthanide ions, the main peak visibly broadens (see Figure S5 for the fitted values), and for some dopants, additional signals corresponding to new local environments appear in the quantitative spectrum. In the f^0−f^5 (La^{3+}−Sm^{3+}) group, two peaks are apparent that shift to lower frequencies as the number of f electrons increases. In the f^6 ion (Eu^{3+}), they overlap, leading to a single apparent peak. In the f^7−f^9 (Gd^{3+}−Dy^{3+}) and f^{11}−f^{12} (Er^{3+}−Tm^{3+}) groups, there are no additional peaks, while a low-intensity peak is visible in Ho^{3+} (f^{10}), Yb^{3+} (f^{13}) and Lu^{3+} (f^{14}). The signal of the Er-doped material is substantially broader and shifted to higher frequencies relative to all of the other materials. The inspection of this data set allows us to draw the following conclusions: (a) the addition of rare earth ions in the +3 oxidation state to $CsPbCl_3$ leads to changes in the atomic-level structure of the host material and, in conjunction with the PRE effects shown above, evidences aliovalent incorporation of the rare earth ions into $CsPbCl_3$; (b) new local environments appear that are characterized by substantially shortened T_1 values and these correspond to Cs^+ sites in close proximity of the Ln^{3+} dopant; (c) the spectral changes are qualitatively the same for La^{3+} (f^0, diamagnetic)

https://doi.org/10.1021/jacs.3c11427
J. Am. Chem. Soc. 2024, 146, 9554−9563

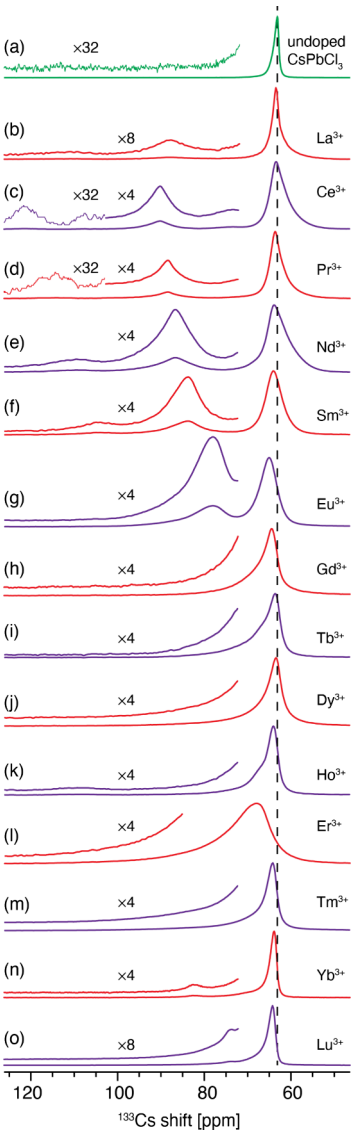

Figure 3. Quantitative ^{133}Cs MAS NMR spectra of bulk mechanochemical $CsPbCl_3$ perovskite compositions: (a) undoped and (b–o) doped with 10 mol % excess $LnCl_3$ (Ln^{3+} given next to each spectrum).

and Ce^{3+}–Eu^{3+} (f^1–f^6) suggesting that they have a common origin which is related to local structural changes rather than paramagnetic effects. This last distinction is subtle but important because paramagnetic doping is well-known to lead to large shifts that qualitatively resemble those seen here. We discuss this point in more detail now.

Paramagnetic (or hyperfine, hf) shifts arise due to two major mechanisms: (a) overlap between the unpaired electron density and the s orbitals of the NMR nucleus (referred to as contact or Fermi shift) and (b) through-space electron–nuclear magnetic dipole interaction (pseudocontact shift, PCS). Since Fermi shifts require orbital overlap, they are common in materials where the paramagnetic ion is covalently bonded to the NMR nucleus, for example in lanthanide pyrochlores, phosphates, and actinide oxides.[58,71−73] They are also present when the NMR nucleus has an ionic bond but is close enough to the paramagnetic species for an orbital overlap to occur. This is common in transition metal compounds, for example, Cs_2CuCl_4,[74] Cs_2CoCl_4,[75] $CsMnCl_3$,[76] or Prussian blue analogues such as $CsNi[Co[CN]_6]$.[77] In lanthanide-doped $CsPbCl_3$, the most likely location for the lanthanide is the B-site, corresponding to aliovalent Pb^{2+} substitution with the concomitant formation of a Cs^+ vacancy, because of the similarity of the ionic radii of Pb^{2+} (119 pm) and Ln^{3+} (86–103 pm). Conversely, aliovalent replacement of Cs^+ (188 pm) with the much smaller lanthanide is unlikely. In the cubic phase of $CsPbCl_3$, the distance between the Cs^+ and Pb^{2+} sites is 485 pm and between two Cs^+ sites 560 pm. This hypothesis has recently been corroborated by atomic-scale STEM EDX mapping of Yb-doped $CsPbCl_3$ which evidenced that Yb^{3+} has the capacity to replace Pb^{2+}, in addition to occupying interstitial sites within the perovskite structure.[24] Considering the ionic radii of Cs^+ (188 pm) and Ln^{3+} (86–103 pm) and the limited spatial extent of the 4*f* orbitals, transfer of unpaired electron density from Ln^{3+} to Cs^+ is essentially impossible, regardless of the exact location and type of lanthanide. Indeed, Fermi shifts for lanthanides are typically on the order of thousands of ppm and, for example, in rare earth stannates, span the range between −4000 and +4000 ppm depending on the type of lanthanide ion (see Figure S6 for an example of a hf-shifted ^{133}Cs spectrum).[71]

Pseudocontact shifts result when the paramagnetic lanthanide has an anisotropic magnetic susceptibility, which depends on the symmetry of the local coordination environment. In $CsPbCl_3$, the local environment is highly symmetric when Ln^{3+} occupies the B-site in the cubic phase (octahedral ligand field), which translates to vanishingly small PCS. The magnitude of PCS further depends on the Cs-RE distance, the angle θ between the RE magnetic axis of symmetry and the Cs-RE internuclear axis, and the type of lanthanide through its total angular momentum and *g* factor. Notably, the geometrical dependence of PCS contains a scaling factor of $(3\cos^2\theta - 1)$ which amounts to zero or nearly zero when $\theta = 54.74°$, as is the case in the cubic or nearly cubic phase of $CsPbCl_3$ (Figure S7). We can further exclude the possibility that the new signals appearing in the Ce–Gd group are caused by pseudocontact shifts by comparing the relative magnitudes of the shifts expected for the respective rare earth metal ions on theoretical grounds with those observed experimentally (Figure S8). The relative magnitudes are in clear disagreement (by a factor of 12 for Sm^{3+} and a factor of 2 for Pr^{3+} and Eu^{3+}, scaled to the shift of Ce^{3+}) evidencing that PCS is not the origin of these shifts. An analogous analysis can be done for Fermi shifts, and it also predicts magnitudes which are off by up to a factor of 5 and therefore in disagreement with the data. Finally, Gd^{3+} (f^7) is a special case since it has a half-full 4f shell and as such has a PCS of strictly 0.[35] These results unambiguously indicate that in the La–Gd group of dopants the spectra are dominated by structural rather than paramagnetic effects. In fact, the separation between the original peak of $CsPbCl_3$ and the two new local environments steadily decreases in the La–Gd series in a nearly linear fashion (Figure S9). The key structural parameter that changes in this series is the ionic radius, which decreases as the 4f shell is filled, an effect known as lanthanide contraction. This result suggests that the position of the new peaks is related to the ionic radius of the dopant and may be a proxy of the local octahedral distortion (Figure 4a). Specifically, substituting the smaller lanthanide (86–103 pm) for the larger Pb^{2+} (119 pm) with the concomitant formation of a Cs^+ vacancy (ionic radius of Cs^+: 188 pm) locally increases the octahedral tilting depending on the ionic radius of the lanthanide. That said, the average structure of the materials

https://doi.org/10.1021/jacs.3c11427
J. Am. Chem. Soc. 2024, 146, 9554−9563

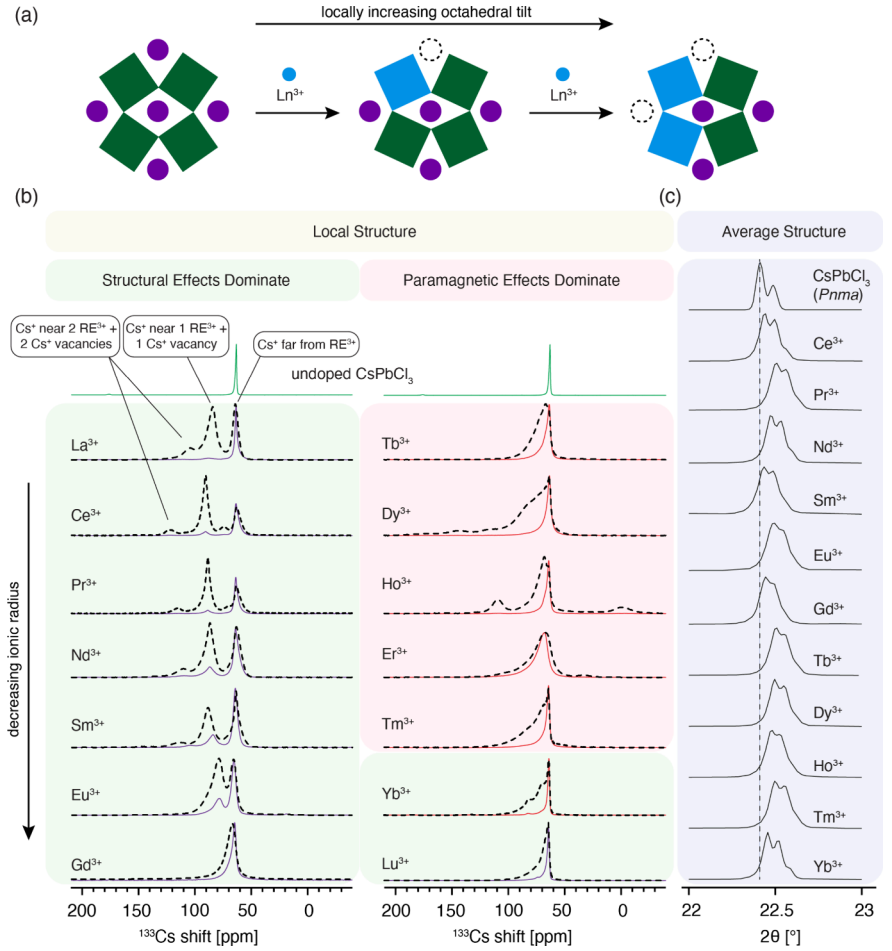

Figure 4. (a) Interpretation of the structural effect leading to the appearance of new ^{133}Cs resonances in $CsPbCl_3$ doped with lanthanides from La^{3+} to Gd^{3+}. The decreasing ionic radius locally tunes the tolerance factor, leading to a gradual increase in the octahedral tilt. (b) Comparison of quantitative (solid lines) and fast-recycling (dashed lines) ^{133}Cs MAS NMR spectra of the materials (a larger version of the figure is given in Figure S15). (c) Powder XRD patterns of selected materials (magnified [121] reflection). The small relative shift of the peak position in the different materials is attributed to experimental uncertainty rather than changes in the average structure.

measured by X-ray diffraction at room temperatures remains monoclinic for all of the materials, indicating that this structural effect operates only in the close proximity of the dopant (Figure 3c).

We used the binomial theorem to calculate the probabilities for different local Cs environments as a function of the lanthanide content and compared them to the experimental peak areas for the two most intense peaks in the quantitative ^{133}Cs spectra. The binomial theorem implies random distribution of the dopants across all the Pb sites. We found that the binomial prediction is in good qualitative agreement for all of the early lanthanide dopants (La^{3+}, Pr^{3+}, Ce^{3+}, Sm^{3+}, Eu^{3+}, 1−20% Nd^{3+}) (Figures S18 and S19). We note, however, that the binomial prediction slightly overestimates the population of the Pb_7Ln local environment relative to that in the experiment. This can be rationalized by considering that the materials studied here are nonstoichiometric (aliovalent substitution, i.e., Pb^{2+} replaced by Ln^{3+}) and the dopants ($LnCl_3$) are added as excess relative to stoichiometric $CsPbCl_3$. The second major source of discrepancy is likely the peak deconvolution process used to quantify the peak areas, especially in the case of Eu^{3+} where the peaks overlap substantially.

The situation is different in the Tb−Yb group, in which the expected relative magnitude of PCSs is 5−10 times larger than for the early lanthanides, owing to their substantially larger total angular momentum. In conjunction with nonideal cancellation of the geometrical factors described above, this may lead to detectable PCS. Because the pseudocontact interaction is anisotropic, the first indication that PCSs may be present is the appearance of many spinning sidebands in the spectrum. This effect is indeed evident for Tb, Dy, Ho, Er and Tm which have more pronounced spinning sidebands than the other lanthanides (Figures S10 and S11, 22 kHz MAS; Figure S12, 5 kHz MAS). That said, while detectable, this effect is relatively small as typical pseudocontact shift anisotropies for Ln^{3+} ions are on the order of thousands of ppm.

For example, the following values have been previously reported: 1500 ppm for Yb_2Sn_2O,[78] 600 ppm ($YbPO_4$), 2800 ppm ($ErPO_4$), and 1700−4000 ppm in other rare earth metal orthophosphates.[79] Here, the anisotropy is at most 200−400 ppm, although a precise fit is not possible due to the additional susceptibility anisotropy effect[78] which makes the spinning sideband manifold a convolution of the two effects.

The signals affected by PCSs can be readily detected because PREs shorten substantially the recovery time of the local environments in the proximity of the rare earth metal ions.

https://doi.org/10.1021/jacs.3c11427
J. Am. Chem. Soc. 2024, 146, 9554−9563

Their signals can therefore be enhanced by recording the spectra using short recycling delays. Figure 4b shows a comparison of the quantitative and fast-recycling spectra for each material. While for La^{3+}-Gd^{3+}, the qualitative picture is the same in both experiments, there are multiple additional signals visible in the Tb^{3+}-Yb^{3+} group with fast recycling. In the case of Ho^{3+} and Er^{3+} they are present on either side of the original $CsPbCl_3$ peak, a tell-tale sign of PCSs, whose relative sign depends on the $(3\cos^2\theta - 1)$ factor and can be either positive or negative depending on the local geometry (see Figure S7). The relatively large shift and broadening of the Er^{3+} material relative to all the other lanthanides (Figure 3l) is likely caused by anisotropic bulk magnetic susceptibility broadening (ABMS) (See Supplementary Note 2 and Figure S23 for a more detailed discussion).[80,81]

We next show that incorporation also occurs for lanthanides in the +2 oxidation state (Sm^{2+} and Eu^{2+}). To that end, we used SmI_2 and EuI_2 as the lanthanide ion precursors. The PRE effect in these samples is analogous to that seen for the Ln^{3+} ions (Figure 2), confirming that changing the oxidation state does not affect the capacity of these ions to incorporate into $CsPbCl_3$. The corresponding ^{133}Cs spectra are qualitatively similar between the two oxidation states, with one (for Eu^{2+}) and two (for Sm^{2+}) extra peaks formed upon doping, the only difference being a small shift to higher frequencies of all the peaks in the case of the +2 dopants caused by the concomitant iodide−chloride mixing (Figure S13).

While ^{133}Cs is the most convenient local structure probe in $CsPbCl_3$, for the sake of completeness, we also explored the effect of lanthanide doping on the ^{207}Pb spectra in the case of Nd^{3+} (Figure S14). The spectrum has two distinct overlapping components, one broad and one narrow, corresponding to local Pb^{2+} environments that are affected by the paramagnetic dopant to a higher and lesser degree, respectively. The distribution of T_1 values across the line shape corroborates this interpretation, with the broad part of the spectrum having a 20−50% shorter T_1 than the narrow part. Notably, the ^{207}Pb T_1 relaxation data sets take considerably longer to acquire (∼12 h, compared to 2−4 h for ^{133}Cs). Considering the time requirements, higher signal-to-noise ratio, and higher resolution of the ^{133}Cs data sets, we conclude that ^{133}Cs should be the nucleus of choice for studying paramagnetic effects in cesium halometalates.

In conclusion, we have shown that all of the rare earth metal ions have the capacity to incorporate into the perovskite structure of $CsPbCl_3$, in both the +3 and +2 oxidation states.

We found that the incorporation of lanthanides leads to paramagnetic NMR effects detectable in the ^{133}Cs NMR signal of the perovskite phase. Those effects include the appearance of additional signals associated with Cs^+ sites in close proximity of the lanthanide, in addition to substantial shortening of the ^{133}Cs longitudinal relaxation times, T_1. Faster relaxation is also observed for incorporation of the diamagnetic lanthanides, La^{3+} and Lu^{3+}, where we attribute it to enhanced dipolar relaxation induced by the ^{139}La and ^{175}Lu nuclear spins. In the case of the paramagnetic lanthanides, the 5−425 times faster T_1 is caused by paramagnetic relaxation enhancement due to the through-space dipolar interaction between the unpaired 4f electrons and the ^{133}Cs nuclear spins. In all cases, there is a nonuniform distribution of T_1 values across the spectrum, which is strongly dependent on the lanthanide ion loading.

Our analysis indicates that the nearly linear changes in the ^{133}Cs shifts observed for doping with the lanthanides from La^{3+} through Gd^{3+} are dominated by structural rather than paramagnetic effects. We suggest they are determined by the radius of the lanthanide ion rather than its magnetic properties, and therefore are a proxy of the local octahedral distortion.

On the other hand, for the lanthanides between Tb^{3+} and Tm^{3+}, paramagnetic effects dominate, and we attribute the changes in the ^{133}Cs NMR spectrum to pseudocontact shifts. We find no evidence of contact (Fermi) shifts on ^{133}Cs, indicating that there is no significant overlap of the unpaired 4f electron spin density with the Cs^+ site.

One of the important future areas of study will be the use of computational methods to fully assign ^{133}Cs MAS NMR spectra of paramagnetically doped halide perovskites. These computations are expected to be demanding, owing to the need for fully relativistic treatment and inclusion of spin−orbit coupling. In the context of aliovalent doping, the key challenge will be to identify the possible structural models: Are the chloride ions involved in charge compensation? Do the vacancies cause a local distortion of symmetry leading to multiple possible inequivalent lanthanide positions? Answering these questions will go a long way toward understanding aliovalent doping in this class of solids.

Our work shows that solid-state NMR of metal halide perovskites doped with lanthanides is a highly sensitive indicator of the dopant incorporation, loading, and interaction with the perovskite structure. We expect the framework developed here to aid in atomic-level characterization of optoelectronic materials with this remarkably diverse and technologically significant class of dopants.

■ ASSOCIATED CONTENT

Data Availability Statement

The raw NMR and XRD data are available on Zenodo: https://zenodo.org/records/10853121.

Supporting Information

The Supporting Information is available free of charge at https://pubs.acs.org/doi/10.1021/jacs.3c11427.

XRD, additional NMR analysis, additional NMR spectra, and relaxation data (PDF)

■ AUTHOR INFORMATION

Corresponding Authors

Dominik J. Kubicki − *School of Chemistry, University of Birmingham, B15 2TT Birmingham, U.K.;* orcid.org/0000-0002-9231-6779; Email: d.j.kubicki@bham.ac.uk

Lyndon Emsley − *Laboratory of Magnetic Resonance, Institute of Chemical Sciences and Engineering, Ecole Polytechnique Fédérale de Lausanne (EPFL), CH-1015 Lausanne, Switzerland;* orcid.org/0000-0003-1360-2572; Email: lyndon.emsley@epfl.ch

Authors

Daniel Prochowicz − *Institute of Physical Chemistry, Polish Academy of Sciences, 01-224 Warsaw, Poland;* orcid.org/0000-0002-5003-5637

Albert Hofstetter − *Laboratory of Magnetic Resonance, Institute of Chemical Sciences and Engineering, Ecole Polytechnique Fédérale de Lausanne (EPFL), CH-1015 Lausanne, Switzerland*

Amita Ummadisingu − *Manufacturing Futures Laboratory, Department of Chemical Engineering, University College London, WC1E 7JE London, United Kingdom*

https://doi.org/10.1021/jacs.3c11427
J. Am. Chem. Soc. 2024, 146, 9554−9563

Complete contact information is available at:
https://pubs.acs.org/10.1021/jacs.3c11427

Notes

The authors declare no competing financial interest.

■ ACKNOWLEDGMENTS

D.J.K. acknowledges the UKRI Horizon Europe guarantee funding (PhotoPeroNMR, Grant Agreement EP/Y01376X/1). This work was supported by Swiss National Science Foundation Grant 200020_212046. D.P. acknowledges the National Centre for Research and Development (Project V4-JAPAN/2/14/PeDET/2022) for financial support.

■ REFERENCES

(1) Li, W.; Wang, Z.; Deschler, F.; Gao, S.; Friend, R. H.; Cheetham, A. K. Chemically Diverse and Multifunctional Hybrid Organic-Inorganic Perovskites. *Nat. Rev. Mater.* **2017**, *2*, 16099.

(2) Protesescu, L.; Yakunin, S.; Bodnarchuk, M. I.; Krieg, F.; Caputo, R.; Hendon, C. H.; Yang, R. X.; Walsh, A.; Kovalenko, M. V. Nanocrystals of Cesium Lead Halide Perovskites ($CsPbX_3$, X = Cl, Br, and I): Novel Optoelectronic Materials Showing Bright Emission with Wide Color Gamut. *Nano Lett.* **2015**, *15*, 3692−3696.

(3) Nedelcu, G.; Protesescu, L.; Yakunin, S.; Bodnarchuk, M. I.; Grotevent, M. J.; Kovalenko, M. V. Fast Anion-Exchange in Highly Luminescent Nanocrystals of Cesium Lead Halide Perovskites ($CsPbX_3$, X = Cl, Br, I). *Nano Lett.* **2015**, *15*, 5635−5640.

(4) Akkerman, Q. A.; D'Innocenzo, V.; Accornero, S.; Scarpellini, A.; Petrozza, A.; Prato, M.; Manna, L. Tuning the Optical Properties of Cesium Lead Halide Perovskite Nanocrystals by Anion Exchange Reactions. *J. Am. Chem. Soc.* **2015**, *137*, 10276−10281.

(5) Sun, S.; Yuan, D.; Xu, Y.; Wang, A.; Deng, Z. Ligand-Mediated Synthesis of Shape-Controlled Cesium Lead Halide Perovskite Nanocrystals via Reprecipitation Process at Room Temperature. *ACS Nano* **2016**, *10*, 3648−3657.

(6) Zhang, D.; Eaton, S. W.; Yu, Y.; Dou, L.; Yang, P. Solution-Phase Synthesis of Cesium Lead Halide Perovskite Nanowires. *J. Am. Chem. Soc.* **2015**, *137*, 9230−9233.

(7) Kachhap, S.; Singh, S.; Singh, A. K.; Singh, S. K. Lanthanide-Doped Inorganic Halide Perovskites ($CsPbX_3$): Novel Properties and Emerging Applications. *J. Mater. Chem. C* **2022**, *10* (10), 3647−3676.

(8) Huang, H.; Li, R.; Jin, S.; Li, Z.; Huang, P.; Hong, J.; Du, S.; Zheng, W.; Chen, X.; Chen, D. Ytterbium-Doped $CsPbCl_3$ Quantum Cutters for Near-Infrared Light-Emitting Diodes. *ACS Appl. Mater. Interfaces* **2021**, *13* (29), 34561−34571.

(9) Zeng, M.; Artizzu, F.; Liu, J.; Singh, S.; Locardi, F.; Mara, D.; Hens, Z.; Van Deun, R. Boosting the Er^{3+} 1.5 μm Luminescence in $CsPbCl_3$ Perovskite Nanocrystals for Photonic Devices Operating at Telecommunication Wavelengths. *ACS Appl. Nano Mater.* **2020**, *3* (5), 4699−4707.

(10) Jing, X.; Zhou, D.; Sun, R.; Zhang, Y.; Li, Y.; Li, X.; Li, Q.; Song, H.; Liu, B. Enhanced Photoluminescence and Photoresponsiveness of Eu^{3+} Ions-Doped $CsPbCl_3$ Perovskite Quantum Dots under High Pressure. *Adv. Funct. Mater.* **2021**, *31* (31), 2100930.

(11) Li, X.; Duan, S.; Liu, H.; Chen, G.; Luo, Y.; Ågren, H. Mechanism for the Extremely Efficient Sensitization of Yb^{3+} Luminescence in $CsPbCl_3$ Nanocrystals. *J. Phys. Chem. Lett.* **2019**, *10* (3), 487−492.

(12) Milstein, T. J.; Kroupa, D. M.; Gamelin, D. R. Picosecond Quantum Cutting Generates Photoluminescence Quantum Yields Over 100% in Ytterbium-Doped $CsPbCl_3$ Nanocrystals. *Nano Lett.* **2018**, *18* (6), 3792−3799.

(13) Xu, K.; Chen, D.; Huang, D.; Zhu, H. Thermally Stable Emission from Yb^{3+}-Doped $CsPbCl_3$ Nanocrystals. *J. Lumin.* **2021**, *240*, 118464.

(14) Guvenc, C. M.; Yalcinkaya, Y.; Ozen, S.; Sahin, H.; Demir, M. M. Gd^{3+}-Doped α-$CsPbI_3$ Nanocrystals with Better Phase Stability and Optical Properties. *J. Phys. Chem. C* **2019**, *123* (40), 24865−24872.

(15) Wang, L.; Zhou, H.; Hu, J.; Huang, B.; Sun, M.; Dong, B.; Zheng, G.; Huang, Y.; Chen, Y.; Li, L.; Xu, Z.; Li, N.; Liu, Z.; Chen, Q.; Sun, L.-D.; Yan, C.-H. A Eu^{3+}-Eu^{2+} Ion Redox Shuttle Imparts Operational Durability to Pb-I Perovskite Solar Cells. *Science* **2019**, *363* (6424), 265−270.

(16) Zhou, D.; Liu, D.; Pan, G.; Chen, X.; Li, D.; Xu, W.; Bai, X.; Song, H. Cerium and Ytterbium Codoped Halide Perovskite Quantum Dots: A Novel and Efficient Downconverter for Improving the Performance of Silicon Solar Cells. *Adv. Mater.* **2017**, *29* (42), 1704149.

(17) Roh, J. Y. D.; Smith, M. D.; Crane, M. J.; Biner, D.; Milstein, T. J.; Krämer, K. W.; Gamelin, D. R. Yb^{3+} Speciation and Energy-Transfer Dynamics in Quantum-Cutting Yb^{3+}-Doped $CsPbCl_3$ Perovskite Nanocrystals and Single Crystals. *Phys. Rev. Mater.* **2020**, *4* (10), 105405.

(18) Sun, R.; Lu, P.; Zhou, D.; Xu, W.; Ding, N.; Shao, H.; Zhang, Y.; Li, D.; Wang, N.; Zhuang, X.; Dong, B.; Bai, X.; Song, H. Samarium-Doped Metal Halide Perovskite Nanocrystals for Single-Component Electroluminescent White Light-Emitting Diodes. *ACS Energy Lett.* **2020**, *5* (7), 2131−2139.

(19) Luo, X.; Ding, T.; Liu, X.; Liu, Y.; Wu, K. Quantum-Cutting Luminescent Solar Concentrators Using Ytterbium-Doped Perovskite Nanocrystals. *Nano Lett.* **2019**, *19* (1), 338−341.

(20) Liu, Y.; Rong, X.; Li, M.; Molokeev, M. S.; Zhao, J.; Xia, Z. Incorporating Rare-Earth Terbium(III) Ions into $Cs_2AgInCl_6$:Bi Nanocrystals toward Tunable Photoluminescence. *Angew. Chem., Int. Ed.* **2020**, *59* (28), 11634−11640.

(21) Marin, R.; Jaque, D. Doping Lanthanide Ions in Colloidal Semiconductor Nanocrystals for Brighter Photoluminescence. *Chem. Rev.* **2021**, *121* (3), 1425−1462.

(22) Sun, R.; Zhou, D.; Ding, Y.; Wang, Y.; Wang, Y.; Zhuang, X.; Liu, S.; Ding, N.; Wang, T.; Xu, W.; Song, H. Efficient Single-Component White Light Emitting Diodes Enabled by Lanthanide Ions Doped Lead Halide Perovskites via Controlling Förster Energy Transfer and Specific Defect Clearance. *Light Sci. Appl.* **2022**, *11* (1), 340.

(23) Mir, W. J.; Sheikh, T.; Arfin, H.; Xia, Z.; Nag, A. Lanthanide Doping in Metal Halide Perovskite Nanocrystals: Spectral Shifting, Quantum Cutting and Optoelectronic Applications. *NPG Asia Mater.* **2020**, *12* (1), 1−9.

(24) Xu, W.; Liu, J.; Dong, B.; Huang, J.; Shi, H.; Xue, X.; Liu, M. Atomic-Scale Imaging of Ytterbium Ions in Lead Halide Perovskites. *Sci. Adv.* **2023**, *9* (35), No. eadi7931.

(25) Blasse, G.; Wanmaker, W. L.; ter Vrugt, J. W. Some New Classes of Efficient Eu^{2+}-Activated Phosphors. *J. Electrochem. Soc.* **1968**, *115* (6), 673.

(26) Barry, T. L. Luminescent Properties of Eu^{2+} and Eu^{2+} + Mn^{2+} Activated $BaMg_2Si_2O_7$. *J. Electrochem. Soc.* **1970**, *117* (3), 381.

(27) Sun, J.; Zheng, W.; Huang, P.; Zhang, M.; Zhang, W.; Deng, Z.; Yu, S.; Jin, M.; Chen, X. Efficient Near-Infrared Luminescence in Lanthanide-Doped Vacancy-Ordered Double Perovskite Cs_2ZrCl_6 Phosphors via Te^{4+} Sensitization. *Angew. Chem., Int. Ed.* **2022**, *61* (26), No. e202201993.

(28) George, N. C.; Brgoch, J.; Pell, A. J.; Cozzan, C.; Jaffe, A.; Dantelle, G.; Llobet, A.; Pintacuda, G.; Seshadri, R.; Chmelka, B. F. Correlating Local Compositions and Structures with the Macroscopic Optical Properties of Ce^{3+}-Doped $CaSc_2O_4$, an Efficient Green-Emitting Phosphor. *Chem. Mater.* **2017**, *29* (8), 3538−3546.

(29) Reif, B.; Ashbrook, S. E.; Emsley, L.; Hong, M. Solid-State NMR Spectroscopy. *Nat. Rev. Methods Primers* **2021**, *1*, 2.

(30) Grey, C. P.; Dobson, C. M.; Cheetham, A. K.; Jakeman, R. J. B. Studies of Rare-Earth Stannates by Tin-119 MAS NMR. The Use of Paramagnetic Shift Probes in the Solid State. *J. Am. Chem. Soc.* **1989**, *111* (2), 505−511.

(31) Harazono, T.; Adachi, R.; Kijima, N.; Watanabe, T. ^{89}Y MAS NMR in Red Phosphor, Eu-Doped Y_2O_2S. Assignment of Peaks

Shifted by Paramagnetic Eu^{3+}, Spin Lattice Relaxation Time, and Eu Distribution. *Bull. Chem. Soc. Jpn.* **1999**, *72* (12), 2655−2664.
(32) Harazono, T.; Adachi, R.; Shimomura, Y.; Watanabe, T. Firing Temperature Dependence of Eu Diffusion in Eu-Y_2O_2S Studied by ^{89}Y MAS NMR. *Phys. Chem. Chem. Phys.* **2001**, *3* (14), 2943−2948.
(33) Li, W.; Adlung, M.; Zhang, Q.; Wickleder, C.; Schmedt auf der Günne, J. A Guide to Brighter Phosphors-Linking Luminescence Properties to Doping Homogeneity Probed by NMR. *ChemPhysChem* **2019**, *20* (23), 3245−3250.
(34) George, N. C.; Pell, A. J.; Dantelle, G.; Page, K.; Llobet, A.; Balasubramanian, M.; Pintacuda, G.; Chmelka, B. F.; Seshadri, R. Local Environments of Dilute Activator Ions in the Solid-State Lighting Phosphor $Y_{3-x}Ce_xAl_5O_{12}$. *Chem. Mater.* **2013**, *25* (20), 3979−3995.
(35) Pell, A. J.; Pintacuda, G.; Grey, C. P. Paramagnetic NMR in Solution and the Solid State. *Prog. Nucl. Magn. Reson. Spectrosc.* **2019**, *111*, 1−271.
(36) Pecher, O.; Carretero-Gonzalez, J.; Griffith, K. J.; Grey, C. P. Materials' Methods: NMR in Battery Research. *Chem. Mater.* **2017**, *29* (1), 213−242.
(37) Softley, C. A.; Bostock, M. J.; Popowicz, G. M.; Sattler, M. Paramagnetic NMR in Drug Discovery. *J. Biomol. NMR* **2020**, *74* (6), 287−309.
(38) Bertini, I.; Turano, P.; Vila, A. J. Nuclear Magnetic Resonance of Paramagnetic Metalloproteins. *Chem. Rev.* **1993**, *93* (8), 2833−2932.
(39) Bakhmutov, V. I. Strategies for Solid-State NMR Studies of Materials: From Diamagnetic to Paramagnetic Porous Solids. *Chem. Rev.* **2011**, *111* (2), 530−562.
(40) Karmakar, A.; Dodd, M. S.; Agnihotri, S.; Ravera, E.; Michaelis, V. K. Cu(II)-Doped $Cs_2SbAgCl_6$ Double Perovskite: A Lead-Free, Low-Bandgap Material. *Chem. Mater.* **2018**, *30* (22), 8280−8290.
(41) Aguiar, P. M.; Katz, M. J.; Leznoff, D. B.; Kroeker, S. Natural Abundance ^{13}C and ^{15}N Solid-State NMR Analysis of Paramagnetic Transition-Metal Cyanide Coordination Polymers. *Phys. Chem. Chem. Phys.* **2009**, *11* (32), 6925−6934.
(42) Ouyang, L. M.; Aguiar, P. J.; Batchelor, R.; Kroeker, S. B.; Leznoff, D. A Paramagnetic Cu(I)/Cu(II)/Zn(II) Coordination Polymer with Multiple CN-Binding Modes and Its Solid-State NMR Characterization. *Chem. Commun.* **2006**, No. 7, 744−746.
(43) Kubicki, D. J.; Stranks, S. D.; Grey, C. P.; Emsley, L. NMR Spectroscopy Probes Microstructure, Dynamics and Doping of Metal Halide Perovskites. *Nat. Rev. Chem.* **2021**, *5* (9), 624−645.
(44) Xiang, W.; Wang, Z.; Kubicki, D. J.; Tress, W.; Luo, J.; Prochowicz, D.; Akin, S.; Emsley, L.; Zhou, J.; Dietler, G.; Grätzel, M.; Hagfeldt, A. Europium-Doped $CsPbI_2Br$ for Stable and Highly Efficient Inorganic Perovskite Solar Cells. *Joule* **2019**, *3* (1), 205−214.
(45) Protesescu, L.; Yakunin, S.; Bodnarchuk, M. I.; Krieg, F.; Caputo, R.; Hendon, C. H.; Yang, R. X.; Walsh, A.; Kovalenko, M. V. Nanocrystals of Cesium Lead Halide Perovskites ($CsPbX_3$, X = Cl, Br, and I): Novel Optoelectronic Materials Showing Bright Emission with Wide Color Gamut. *Nano Lett.* **2015**, *15* (6), 3692−3696.
(46) Hume-Rothery, W.; Powell, H. M. On the Theory of Super-Lattice Structures in Alloys. *Z. Für Krist. - Cryst. Mater.* **1935**, *91* (1−6), 23−47.
(47) Kaufman, L.; Bernstein, H. *Computer Calculation of Phase Diagrams with Special Reference to Refractory Metals*; Academic Press Inc.: United States, 1970.
(48) Goldschmidt, V. M. Die Gesetze der Krystallochemie. *Naturwissenschaften* **1926**, *14* (21), 477−485.
(49) Burger, S.; Ehrenreich, M. G.; Kieslich, G. Tolerance Factors of Hybrid Organic-Inorganic Perovskites: Recent Improvements and Current State of Research. *J. Mater. Chem. A* **2018**, *6* (44), 21785−21793.
(50) Pei, Z.; Yin, J.; Hawk, J. A.; Alman, D. E.; Gao, M. C. Machine-Learning Informed Prediction of High-Entropy Solid Solution Formation: Beyond the Hume-Rothery Rules. *Npj Comput. Mater.* **2020**, *6* (1), 1−8.
(51) Pan, G.; Bai, X.; Yang, D.; Chen, X.; Jing, P.; Qu, S.; Zhang, L.; Zhou, D.; Zhu, J.; Xu, W.; Dong, B.; Song, H. Doping Lanthanide into Perovskite Nanocrystals: Highly Improved and Expanded Optical Properties. *Nano Lett.* **2017**, *17*, 8005−8011.
(52) Klug, M. T.; Osherov, A.; Haghighirad, A. A.; Stranks, S. D.; Brown, P. R.; Bai, S.; Wang, J. T.-W.; Dang, X.; Bulović, V.; Snaith, H. J.; Belcher, A. M. Tailoring Metal Halide Perovskites through Metal Substitution: Influence on Photovoltaic and Material Properties. *Energy Environ. Sci.* **2017**, *10* (1), 236−246.
(53) Kubicki, D. J.; Prochowicz, D.; Pinon, A.; Stevanato, G.; Hofstetter, A.; Zakeeruddin, S. M.; Grätzel, M.; Emsley, L. Doping and Phase Segregation in Mn^{2+}- and Co^{2+}-Doped Lead Halide Perovskites from ^{133}Cs and ^{1}H NMR Relaxation Enhancement. *J. Mater. Chem. A* **2019**, *7*, 2326−2333.
(54) Kubicki, D. J.; Prochowicz, D.; Hofstetter, A.; Zakeeruddin, S. M.; Grätzel, M.; Emsley, L. Phase Segregation in Potassium-Doped Lead Halide Perovskites from ^{39}K Solid-State NMR at 21.1 T. *J. Am. Chem. Soc.* **2018**, *140* (23), 7232−7238.
(55) Kubicki, D. J.; Prochowicz, D.; Hofstetter, A.; Saski, M.; Yadav, P.; Bi, D.; Pellet, N.; Lewiński, J.; Zakeeruddin, S. M.; Grätzel, M.; Emsley, L. Formation of Stable Mixed Guanidinium-Methylammonium Phases with Exceptionally Long Carrier Lifetimes for High-Efficiency Lead Iodide-Based Perovskite Photovoltaics. *J. Am. Chem. Soc.* **2018**, *140* (9), 3345−3351.
(56) Kubicki, D. J.; Prochowicz, D.; Hofstetter, A.; Zakeeruddin, S. M.; Grätzel, M.; Emsley, L. Phase Segregation in Cs-, Rb- and K-Doped Mixed-Cation $(MA)_x(FA)_{1-x}PbI_3$ Hybrid Perovskites from Solid-State NMR. *J. Am. Chem. Soc.* **2017**, *139* (40), 14173−14180.
(57) Karmakar, A.; Dodd, M. S.; Zhang, X.; Oakley, M. S.; Klobukowski, M.; Michaelis, V. K. Mechanochemical Synthesis of 0D and 3D Cesium Lead Mixed Halide Perovskites. *Chem. Commun.* **2019**, *55* (35), 5079−5082.
(58) Bertini, I.; Luchinat, C.; Parigi, G.; Ravera, E. *NMR of Paramagnetic Molecules*; Elsevier Science, 2017.
(59) Ran Lim, A.; Gyoo Kim, I. Phase Transition Study by Using ^{133}Cs and ^{207}Pb Nuclear Magnetic Resonance in a $CsPbCl_3$ Single Crystal. *J. Phys. Soc. Jpn.* **2004**, *73* (2), 475−479.
(60) Hayashi, S.; Hayamizu, K. Accurate Determination of NMR Chemical Shifts in Alkali Halides and Their Correlation with Structural Factors. *Bull. Chem. Soc. Jpn.* **1990**, *63*, 913−919.
(61) Zhao, P.; Prasad, S.; Huang, J.; Fitzgerald, J. J.; Shore, J. S. Lead-207 NMR Spectroscopic Study of Lead-Based Electronic Materials and Related Lead Oxides. *J. Phys. Chem. B* **1999**, *103* (48), 10617−10626.
(62) Thurber, K. R.; Tycko, R. Measurement of Sample Temperatures under Magic-Angle Spinning from the Chemical Shift and Spin-Lattice Relaxation Rate of ^{79}Br in KBr Powder. *J. Magn. Reson.* **2009**, *196* (1), 84−87.
(63) Lowe, I. J.; Tse, D. Nuclear Spin-Lattice Relaxation via Paramagnetic Centers. *Phys. Rev.* **1968**, *166* (2), 279−291.
(64) Tse, D.; Hartmann, S. R. Nuclear Spin-Lattice Relaxation Via Paramagnetic Centers Without Spin Diffusion. *Phys. Rev. Lett.* **1968**, *21* (8), 511−514.
(65) Mark Henrichs, P.; Cofield, M. L.; Young, R. H.; Michael Hewitt, J. Nuclear Spin-Lattice Relaxation via Paramagnetic Centers in Solids. ^{13}C NMR of Diamonds. *J. Magn. Reson. 1969* **1984**, *58* (1), 85−94.
(66) Björgvinsdóttir, S.; Walder, B. J.; Pinon, A. C.; Emsley, L. Bulk Nuclear Hyperpolarization of Inorganic Solids by Relay from the Surface. *J. Am. Chem. Soc.* **2018**, *140* (25), 7946−7951.
(67) Lubach, J. W.; Xu, D.; Segmuller, B. E.; Munson, E. J. Investigation of the Effects of Pharmaceutical Processing Upon Solid-State NMR Relaxation Times and Implications to Solid-State Formulation Stability. *J. Pharm. Sci.* **2007**, *96* (4), 777−787.
(68) Ashbrook, S. E.; Griffin, J. M.; Johnston, K. E. Recent Advances in Solid-State Nuclear Magnetic Resonance Spectroscopy. *Annu. Rev. Anal. Chem.* **2018**, *11* (1), 485−508.

https://doi.org/10.1021/jacs.3c11427
J. Am. Chem. Soc. 2024, 146, 9554−9563

(69) Alaimo, M. H.; Roberts, I. E. Effects of Paramagnetic Cations on the Nonexponential Spin-Lattice Relaxation of Rare Spin Nuclei in Solids. *Solid State Nucl. Magn. Reson.* **1997**, *8* (4), 241−250.
(70) Hartman, J. S.; Narayanan, A.; Wang, Y. Spin-Lattice Relaxation in the 6H Polytype of Silicon Carbide. *J. Am. Chem. Soc.* **1994**, *116* (9), 4019−4027.
(71) Grey, C. P.; Dobson, C. M.; Cheetham, A. K.; Jakeman, R. J. B. Studies of Rare-Earth Stannates by ^{119}Sn MAS NMR. The Use of Paramagnetic Shift Probes in the Solid State. *J. Am. Chem. Soc.* **1989**, *111* (2), 505−511.
(72) Martel, L.; Magnani, N.; Vigier, J.-F.; Boshoven, J.; Selfslag, C.; Farnan, I.; Griveau, J.-C.; Somers, J.; Fanghänel, T. High-Resolution Solid-State Oxygen-17 NMR of Actinide-Bearing Compounds: An Insight into the 5f Chemistry. *Inorg. Chem.* **2014**, *53* (13), 6928−6933.
(73) Clément, R. J.; Pell, A. J.; Middlemiss, D. S.; Strobridge, F. C.; Miller, J. K.; Whittingham, M. S.; Emsley, L.; Grey, C. P.; Pintacuda, G. Spin-Transfer Pathways in Paramagnetic Lithium Transition-Metal Phosphates from Combined Broadband Isotropic Solid-State MAS NMR Spectroscopy and DFT Calculations. *J. Am. Chem. Soc.* **2012**, *134* (41), 17178−17185.
(74) Lim, A. R.; Hong, K. S.; Jeong, S.-Y. Nuclear Magnetic Resonance and Transferred Hyperfine Interaction Study of the Crystallographically Inequivalent Cs(I) and Cs(II) in a Cs_2CuCl_4 Single Crystal. *J. Phys. Chem. Solids* **2004**, *65* (7), 1373−1378.
(75) Lim, A. R.; Jung, J. K. Phonon Processes and the Spin-Lattice Relaxation of Two Inequivalent Cs Sites in Cs_2CuCl_4 and Cs_2CoCl_4 Single Crystals. *Solid State Commun.* **2004**, *132* (6), 393−398.
(76) Lim, A. R.; Choh, S. H.; Jeong, S.-Y. Nuclear Magnetic Resonance of ^{133}Cs in a $CsMnCl_3$ Single Crystal. *J. Phys.: Condens. Matter* **1994**, *6* (46), 10141.
(77) Köhler, F. H.; Storcheva, O. Paramagnetic Prussian Blue Analogues $CsM^{II}[M^{III}(CN)_6]$. The Quest for Spin on Cesium Ions by Use of ^{133}Cs MAS NMR Spectroscopy. *Inorg. Chem.* **2015**, *54* (14), 6801−6806.
(78) Grey, C. P.; Dobson, C. M.; Cheetham, A. K. Susceptibility Matching in MAS NMR. The Determination of Hyperfine Tensors from Paramagnetic Stannates. *J. Magn. Reson. 1969* **1992**, *98* (2), 414−420.
(79) Bose, M.; Bhattacharya, M.; Ganguli, S. ^{31}P NMR Studies of Transferred Hyperfine Effects in Rare-Earth Orthophosphates. *Phys. Rev. B* **1979**, *19* (1), 72−80.
(80) Vanderhart, D. L.; Earl, W. L.; Garroway, A. N. Resolution in ^{13}C NMR of Organic Solids Using High-Power Proton Decoupling and Magic-Angle Sample Spinning. *J. Magn. Reson. 1969* **1981**, *44* (2), 361−401.
(81) Alla, M.; Lippmaa, E. Resolution Limits in Magic-Angle Rotation NMR Spectra of Polycrystalline Solids. *Chem. Phys. Lett.* **1982**, *87* (1), 30−33.

https://doi.org/10.1021/jacs.3c11427
J. Am. Chem. Soc. 2024, 146, 9554−9563